

Fluid inclusions in natron - a window into the interior of Enceladus

Liam Perera

liam.perera@diamond.ac.uk

Diamond Light Source <https://orcid.org/0000-0003-2755-8461>

James Le Houx

Rutherford Appleton Laboratory <https://orcid.org/0000-0002-1576-0673>

Alberto Leonardi

Diamond Light Source

Sarah Day

Diamond Light Source

Stephen Thompson

Diamond Light Source

Physical Sciences - Article

Keywords: Enceladus, Fluid inclusions, Natron, Astrobiology, Correlative X-ray tomography and diffraction, In-situ freezing

Posted Date: February 20th, 2026

DOI: <https://doi.org/10.21203/rs.3.rs-8406896/v1>

License:   This work is licensed under a Creative Commons Attribution 4.0 International License.

[Read Full License](#)

Additional Declarations: There is **NO** Competing Interest.

Fluid inclusions in natron - a window into the interior of Enceladus

Liam J. Perera^{1,*}, James Le Houx^{2,3,4}, Alberto Leonardi^{1,5,6}, Sarah J. Day¹, and Stephen P. Thompson¹

¹Diamond Light Source, Rutherford Appleton Laboratory, Didcot, OX11 0DE, United Kingdom

²University of Greenwich, Old Royal Naval College, Park Row, London, SE10 9LS, United Kingdom

³ISIS Neutron & Muon Source, Rutherford Appleton Laboratory, Didcot, OX11 0QX, United Kingdom

⁴The Faraday Institution, Harwell Science and Innovation Campus, Didcot, OX11 0RA, United Kingdom

⁵Friedrich-Alexander-Universität Erlangen-Nürnberg, Technische Fakultät, Erlangen, Germany

⁶Indiana University, Department of Earth and Atmospheric Sciences, Bloomington, 1001 East 10th Street, USA

*corresponding author: Liam Perera (liam.perera@diamond.ac.uk)

ABSTRACT

Saturn's moon Enceladus is a priority target for both NASA Flagship and ESA L4 class missions, as it possesses the three essential ingredients for life: liquid water, a source of energy, and all essential (CHNOPS) elements. As Enceladus's ice crust is geologically active, future missions must understand its habitability through the lens of cryo geochemistry; yet the phase behaviour of Enceladus-type solutions is poorly constrained. Here, we investigate the freezing behaviour of an Enceladus-type Na-Cl-CO₃ solution using combined synchrotron X-ray computed microtomography and diffraction. We report the first observation of fluid inclusions in cryogenic natron (Na₂CO₃ · 10H₂O), a mineral predicted to be present on and within Enceladus. We show that natron precipitation traps and preserves pockets of parent fluid, providing a window into the geochemistry of Enceladus's interior and establishing natron as a mineral of high astrobiological importance. Consequently, we argue that future missions must have the capability to identify surface natron and that direct sampling should prioritize these deposits for their potential to trap and preserve signatures of life.

Keywords: Enceladus, Fluid inclusions, Natron, Astrobiology, Correlative X-ray tomography and diffraction, In-situ freezing.

Introduction

Enceladus, a moon of Saturn, displays geophysical and geochemical evidence of recent and ongoing geological activity^{1,2}. The most dramatic evidence of activity is the presence of distinct jets, feeding a large plume that emanates from the South Polar Terrain (SPT)^{1,3-5}. These plumes contain ice⁶, volatile gases⁷, inorganic salts⁸ and evidence of all six CHNOPS elements^{9,10}. Multiple hypothetical plume mechanisms connect the source of these plumes with a subsurface liquid water ocean^{8,11,12}. Consequently, Enceladus is a prime location for the search for life beyond Earth and is the designated target for both a NASA Flagship-class and an ESA-L4 mission.

We are unlikely to get a direct sample from Enceladus's ocean as the closest estimates place it at least several kilometers deep^{11,13}. However, transport processes in the crust can move ocean-derived material across the solid-liquid phase boundary, bringing it to the surface¹⁴. Samples can therefore be taken from the surface or the plumes to reveal geochemical information about the ocean below.

When an aqueous solution cools and solidifies, the solubility limits of the dissolved components are exceeded, and they precipitate out as solids. As Enceladus's surface temperatures range from 75 K potentially up to 223 K near the plume source¹⁵, most ocean signatures will be solid or hosted in solid matrices. The solid phases in a frozen sample, if not exogenously deposited, would be related to the dissolved components in the original parent fluid. Information about the ocean chemistry can therefore be extracted from surface and plume solid-phase geochemistry. Microscale analysis of the precipitating minerals, their texture, and their petrology can unravel the complexities by acting as a record of subsurface temperature and pressure conditions. The analysis of the surface mineralogy and petrology can then be used to reconstruct interior conditions and, therefore, habitability.

Due to Enceladus's astrobiological importance, a primary science objective is to look for signatures of life on the surface^{16,17}. The low pressure and radiation environment on the surface of Enceladus are likely damaging but not limiting to the detection of the signatures of life^{17,18}. Therefore, to understand how biological signatures could reach and be preserved on the surface, there must be inorganic systems or processes that can act to preserve or protect potential biological material.

37 Mineral hosted fluid inclusions are commonly observed within evaporitic salts^{19,20}, and several salts systems have been
38 found with viable microbes trapped within fluid inclusions^{21–23}. To the best of our knowledge, there have been no recorded
39 observations of fluid inclusions within a cryogenic salt. If present in salts on an icy moon surface, these inclusions would
40 be relatively protected from the deleterious effects of the space environment compared to being hosted in ice. Endogenous
41 cryogenic minerals, forming from aqueous precipitation within Enceladus, could potentially trap biological material, and
42 therefore, would represent a high-priority target inorganic geochemical signature for remote observation.

43 Sodium chloride and sodium carbonate are the main constituents of Enceladus's geochemistry^{8,24}. Throughout the solar
44 system, icy body-associated carbonate salts have also been identified on Bennu²⁵, Ryugu²⁶, Ceres²⁷, and Ariel²⁸. As carbonate
45 salts have low solubility at low temperatures²⁹, they are some of the first cryogenic minerals to form during freezing and
46 therefore have the potential to trap primitive fluid geochemistries. Given the importance of carbonate chemistry on Enceladus,
47 we explore the freezing behaviour of an Enceladus-type, Na-Cl-CO₃ solution in real time using combined synchrotron X-ray
48 computed micro-tomography (μ CT) and diffraction (XRD). We show, for the first time, the widespread presence of primary
49 fluid inclusions in cryogenic Na₂CO₃ · 10H₂O (natron). We discuss the potential implications for rheological processes on
50 Enceladus and other carbonate bearing icy bodies. We propose that direct sampling missions should target these salts due to
51 their potential to trap primary ocean fluids or biosignatures if they are present.

52 Results

53 Cryogenic phase evolution and texture

54 Time resolved tomography and diffraction were collected on K11-DIAD (Diamond Light Source, UK) during the freezing
55 (268 K to 205 K at 6 K/min) of an Na-Cl-CO₃ solution (1 *m* NaCl, 0.5 *m* Na₂CO₃). K11 operates with two independently
56 configurable X-ray beams that allow the collection of spatially correlated imaging and diffraction data (Figure 1A). This
57 study revealed the solidification of an Na-Cl-CO₃ solution using time-resolved diffraction (Figure 1B and D) and tomography
58 (Figure 1C), and identified the solid phases present using the diffraction data.

59 Three solid phases were identified and segmented from the imaging data of the final frozen sample: hexagonal ice (Figure 1E
60 Left); the eutectic phase, comprised of ice, natron, and hydrohalite (Figure 1E Middle); and individual natron crystals (Figure 1E
61 Right).

62 Hexagonal ice was the dominant solid phase, making up 75% of the imaged volume. The basal plane represents a slow-
63 growth face of ice, and dendritic growth proceeds preferentially along the <100> and <112> directions^{30,31}. This was evident
64 in our diffraction data as an under-representation of basal reflections (Figure 1B) and the spotty, single-crystal reflections in
65 our raw diffraction data (Figure 1D). Our imaging data revealed that the ice grew dendritically down the axis of the capillary
66 with the direction of cooling (Figure 1C). As a result, the dimensions and aspect of the crystals in the plane of the beam
67 coupled with the small beam size produce strong single crystal reflections. We therefore limited our diffraction analysis to
68 phase identification with Pawley refinement³² which is intensity independent. The final quenched sample is assumed to be
69 representative of all phases present.

70 The eutectic phase, a mixture of ice and hydrohalite, and natron, made up 4% of the imaged volume. This represents the
71 solidified brine network, of eutectic composition, present in the ice mass. Of the eutectic volume, 3.8% was disconnected from
72 the main eutectic mass, corresponding to 0.07% of the total imaged volume. Individual structure within this phase was not
73 resolvable with imaging. The appearance of rings from a previously spotty pattern at 245 K in the raw diffraction was caused by
74 the formation of multiple small crystallites (Figure 1C and D). The scattering signal from hydrohalite appeared at this eutectic
75 temperature and its powder-like scattering (clear rings), suggests it precipitated as a fine-grained mass.

76 The final major solid phase was subhedral crystals of sodium carbonate in the form of natron (Figure 1A Right). This phase
77 made up 21% of the imaged volume. Similarly to the ice crystals, the small beam and crystal dimensions produced spotty single
78 crystal reflections. DIAD's geometry only interacts with a reduced spherical arc of the Ewald sphere and the sample does not
79 spin during collection, preventing the reconstruction of a complete intensity profile. The presence of natron is evident in some
80 diffraction scans at 205 K (Figure 2A and B). This was due to the population of randomly oriented, smaller crystals (Figure 2C)
81 present at the bottom of the imaged volume producing a more powder-like signal.

82 In our imaged volume there were two separate habits of natron that form over time. Firstly, large subhedral grains
83 precipitated and grew before ice formation. After the onset of ice formation, the subhedral carbonate crystals remained trapped
84 within the mass of ice and their elongated profile prevented further movement. These natron crystals appear to be randomly
85 oriented (Figure 2D). Once the ice encapsulated large grains, smaller secondary offshoots of natron formed from larger crystals
86 and were templated by the ice structure (Figure 2E).

87 The petrology of the natron can be used to reconstruct its evolution. The presence of large subhedral crystals suggests that
88 they grew unconfined and once contained by ice, the growth is inhibited, which can be seen in the salt phase volume in Figure
89 1F. The initial growth of the ice leads to a temporary interruption to the growth of the natron. These events are recorded in the

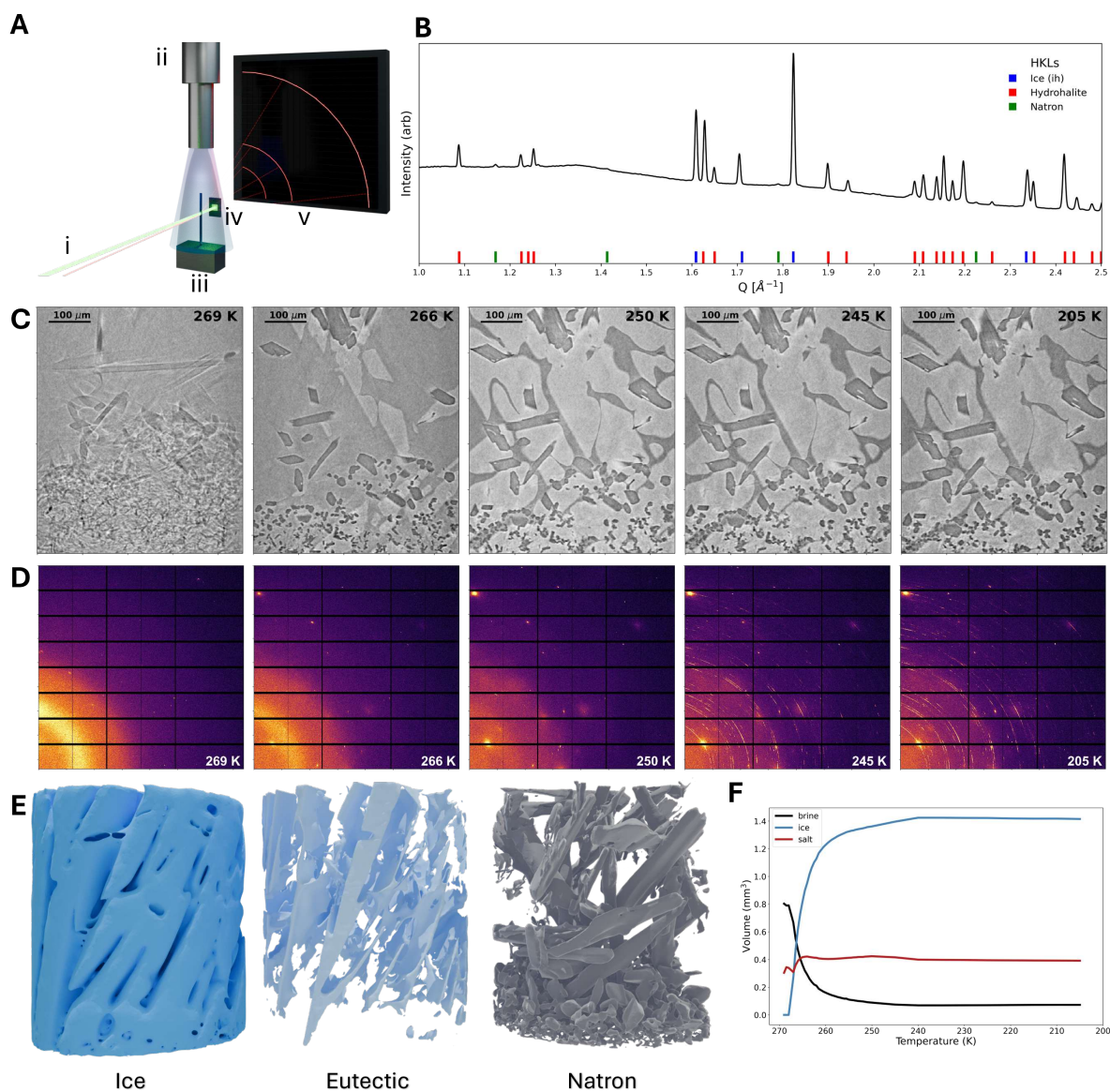


Figure 1. Identification of major phases and structure during real time freezing of an Na-Cl-CO₃ solution. (A) Rendering of the experimental setup with dual beams (i) cryostream (ii) cooling the capillary sample (iii) and collection of imaging (iv) and diffraction (v) data. (B) Summed diffraction pattern from a 10 × 10 grid scan in final scan at 205 K showing locations of refined reflections of ice, hydrohalite, and natron using the Pawley method. (C) Reconstructed XY slice vs temperature showing the growth of each phase and development of the final microstructure. (D) Corresponding 2D diffraction patterns for central point in C showing texture evolution. (E) Rendered volumes of ice, the eutectic phase, and natron in final scan at 205 K (F) Plot of evolution of volume of each phase with temperature calculated from segmented volumes

90 natron petrology. In a more complex aqueous system, as we may expect of Enceladus's ocean, the microscale context of a
 91 mineral's crystallisation can be used to construct a more comprehensive view of the evolution of a cryogenic system.

92 Rheological implications for the ice crust

93 The presence of non-ice material will affect the strength and deformation behaviour of the ice crust. In the ductile regime,
 94 grain boundary sliding and creep have been shown to be inhibited by the presence of fine-grained material^{33–35}. This leads
 95 to the mechanical strengthening of ice and the increase in yield strength. In the brittle regime however, the presence of gas
 96 pockets or brine networks can promote crack propagation^{31,36}. The orientation of ice crystals is also known to produce strong

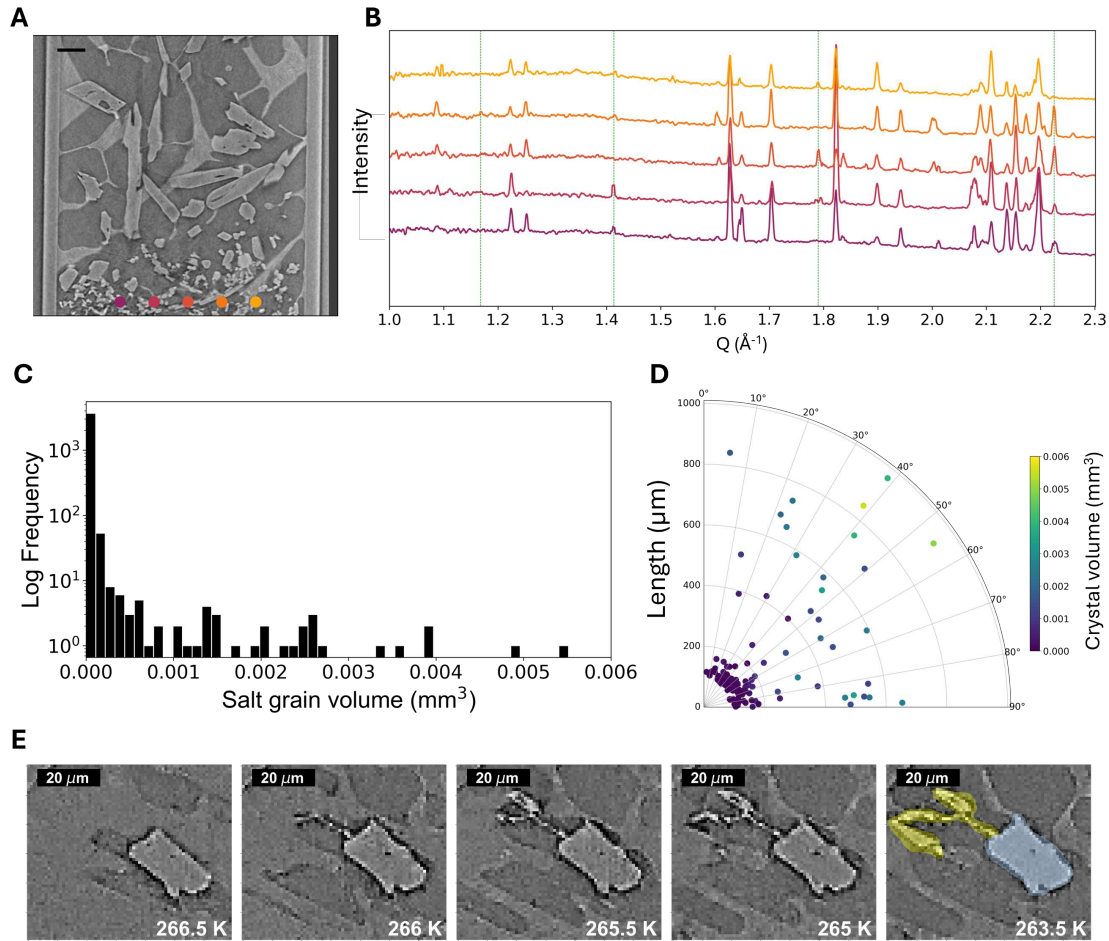


Figure 2. Results of spatially resolved diffraction probing an Na-Cl-CO₃ ice mixture at 205 K. (A) Location of individual diffraction patterns in the reconstructed volume; the scale bar is 100 μm . (B) Resulting color-coded diffraction patterns showing the location of natron reflections (green lines). (C) Size distribution of separated salt grains in the final quenched sample (205 K). (D) Polar plot showing the orientation in relation to the z-axis and volume (colour) of the salt crystal c-axis for crystals with a volume above $1 \times 10^{-4} \text{ mm}^3$. (E) Evolution of a secondary natron precipitation event (Yellow) additional to the primary crystal (Blue), displayed as an XY slice in the reconstructed volume.

97 anisotropy in the mechanical behaviour of ice masses, leading to strengthening along the axis of oriented crystals and weakening
 98 in the perpendicular direction³¹. The morphology and orientation of natron crystals we observe will impact ice rheology
 99 and mechanical behaviour on Enceladus, and compositional heterogeneities will lead to mechanical heterogeneities. Due
 100 to the temperatures on Enceladus multiple solid phases may precipitate and therefore may have a meaningful impact on the
 101 mechanical behaviour of the crust.

102 On Ceres, a much larger icy body than Enceladus, hydrated Sodium carbonate is observed in impact craters³⁷. The
 103 morphology of the craters, and lack of degradation given their ages suggest that the surface of Ceres is much stronger than pure
 104 ice and contains a large amount of non-ice material^{38,39}. Our work, coupled with the observation that natron is found in impact
 105 craters on Ceres, suggests that an ice mix of interstitial hydrated sodium carbonate could have different viscosities compared to
 106 pure ice which could explain observations of slow surface relaxations⁴⁰.

107 Primary fluid entrapment in cryogenic natron

108 In this Na-Cl-CO₃ system, we found the widespread presence of fluid inclusions within the sub-hedral natron crystals
 109 (Figure 3A). This is, to the best of our knowledge, the first time that fluid inclusions have been observed non-destructively in
 110 cryogenic salts. μCT imaging combined with XRD gives us a non-destructive way to identify the microstructure of the natron
 111 in-situ.

112 The inclusions identified were a mix of primary, intra-granular, and pseudo-inclusions (cavities)(Figure 3C). As the inclusion
 113 size were at the limits of our imaging resolution, we did not observe their freezing but would expect that they would be frozen
 114 at the same eutectic temperature as the parent fluid. As all inclusions formed during formation and growth of the host grain,
 115 they can be classified as primary inclusions (Figure 3B). No re-crystallisation of natron was observed. Larger salt grains were
 116 more likely to contain inclusions and would contain larger inclusions (Figure 3C). Of the separated salt grains (n=3779), 3%
 117 contained fluid inclusions. However, within grains larger than $1 \times 10^{-4} \text{ mm}^3$ 58% contained inclusions and 100% contained
 118 inclusions in grains above $1 \times 10^{-3} \text{ mm}^3$ (n=29). It is important to note that the particle size distribution (Figure 2C) and
 consequently our size sampling dominates this observed relationship as there were fewer large crystals in our imaged volume.

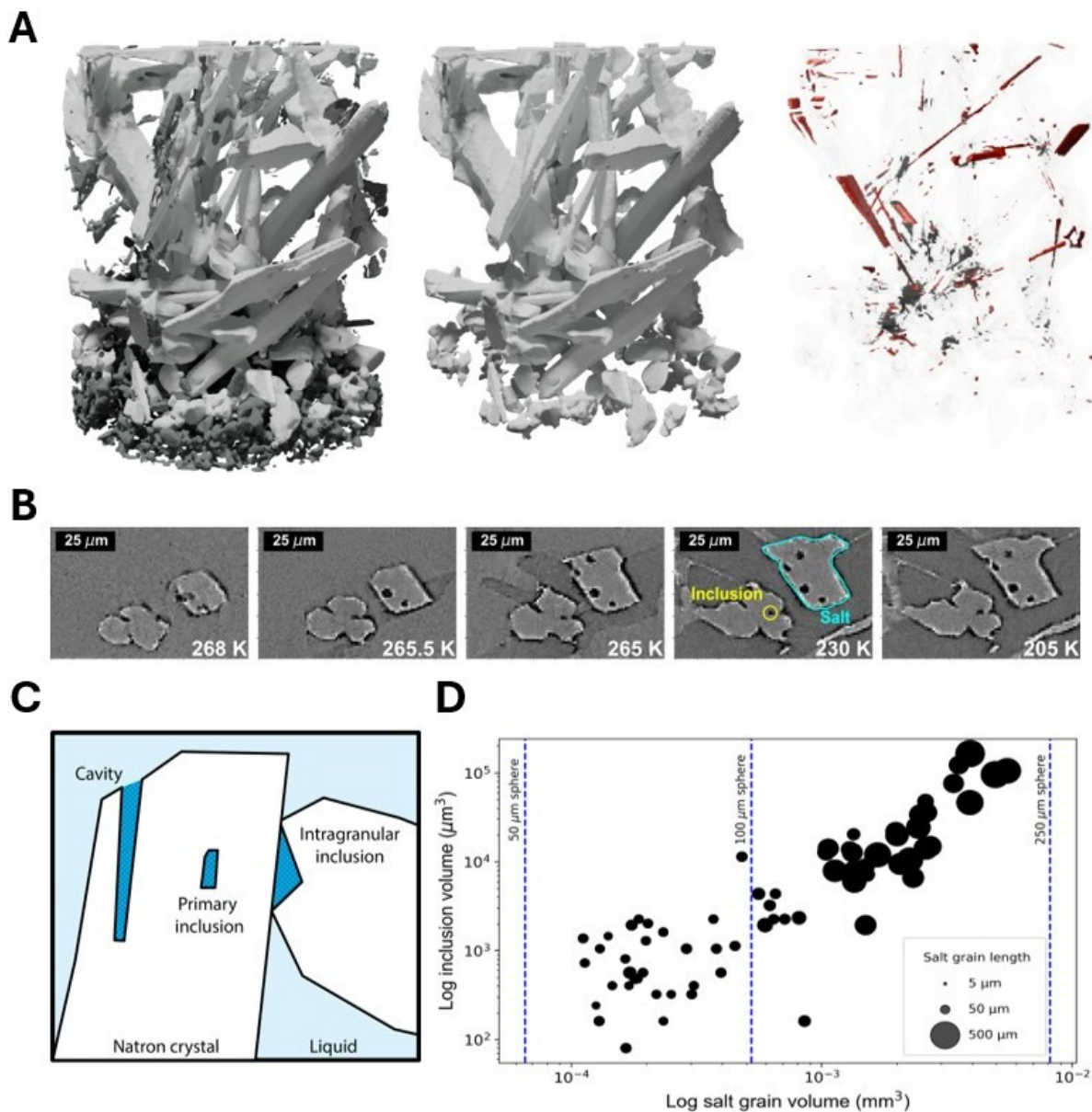


Figure 3. Analysis of precipitated natron and its inclusions. (A) Rendering of segmented salt particles. Particles with a volume above $1 \times 10^{-3} \text{ mm}^4$ are displayed in white, with their associated inclusions shown in red. Salts not included in the analysis are shown as brown. (B) Example of a primary fluid inclusion enclosure, from reconstructed XY slices. A natron crystal (blue) and an associated inclusion (yellow) are labeled (C) Schematic representation of the types of inclusions we observed in the natron crystals. (D) The size of the host grain versus the size of its associated inclusion. The size of each point represents the long axis length of the natron crystal. The volume of equivalent spheres are displayed as dashed lines for reference.

Discussion

Plume transport and surface deposition

Enceladus provides access to interior geochemical information through the eruption of sustained cryovolcanic plumes around its southern pole^{1,3}. The exact mechanism with which material reaches the surface is not known but it is clear that the geochemistry of the plume requires that some portion of the material originates from dispersion of a liquid source^{24,41,42}. A water-filled fissure within the ice crust, exposed by tidal forces^{43,44}, leads to rapid depressurization and acceleration of the gas phase, leading to drag transport of particles out into space. Boiling and exsolution of the liquid source creates dispersed droplets that are cooled and freeze as they are transported⁴⁵. The plumes of Enceladus have already been proposed as high-priority for life detection experiments⁴⁶⁻⁴⁸. Our work suggests that plume deposits should be explored for signs of natron due to its potential to trap ocean fluids (Figure 4).

In figure 2D, the largest long-axis of the natron crystals we observe is 485 μm and the smallest is 34.3 μm , although our analysis of crystals was limited to particles larger than 0.0001 mm^3 . The effect of confinement prevents the further growth of natron suggesting that the diameter of a dispersed droplet would place an upper limit on the size of the precipitating natron crystals. The cooling rate of a dispersed droplet would further control the size of the natron crystal, with larger droplets cooling more slowly, leading to larger natron crystals. Our final imaged volume was 0.91 mm^3 which is equivalent to a sphere of approximately 600 μm in diameter while the longest crystal axis we observed was 485 μm . As the long axis of this largest crystal was oriented at 38 degrees, it is more appropriate to set the long axis of our volume (1.2 mm) as the confining length. Therefore, we may expect that large crystals would require droplet diameters closer to that of the long axis of our imaged volume. It should be noted that the majority of detected plume particles by Cassini were micrometer to nanometer sized^{49,50}. However, Cassini's closest fly-by (25 km) would not have been able to capture larger particles due to the gravity size sorting that prevents larger particle reaching Cassini's lowest fly-by altitude. Remote observation suggests larger surface grain sizes can be found closer to the plume sources⁵¹, and gas-particle acceleration models suggest that particles of up to 2 mm could be ejected close to the plume vents⁵². Near-vent plume deposits, potentially supplied by larger plume particles, should therefore be investigated for natron (Figure 4 A).

Preservation of biosignatures in natron

To our knowledge, there have been no studies examining the preservation and viability of microbes within cryogenic salts. Inclusion formation is widely reported in evaporitic salt deposits^{19,20}. As these salts precipitate from solution, defects and imperfections, or excessive under-cooling, can lead to irregular growth of the solid interface¹⁹. The timing of enclosure is largely kinetic, so these inclusions preserve a range of chemistries that track the evolution of the system.

Fluid inclusions are a rich source of geochemical information, as they trap fluid at the time of formation. Fluid inclusions in halite, a common evaporite mineral on Earth, have been used to reconstruct past ocean water physiochemistry⁵³. Inclusion analysis is complex and requires multi-modal instrumentation. Any study of fluid inclusions requires petrological and paragenetic analysis to determine the timing of inclusion formation⁵⁴. It is unlikely that the necessary instrumentation for inclusion analysis will reach Enceladus. However, direct sampling and analysis of salt rich materials must appreciate the potential for these inclusions to impact sensitive chemical measurements. More importantly, many salt-hosted fluid inclusions have been found with organic biological signatures^{55,56} and even trapped microorganisms^{21-23,57-59}. If microbial life is present in the ocean of Enceladus, then the precipitation of natron has the potential to trap life or signatures of life in fluid inclusions.

Once present at- or near the surface of Enceladus, natron may enhance the preservation of geochemical and biological signatures, if present. The higher density of natron (1.46 g cm^{-3}) compared to ice at $\sim 73\text{ K}$ (0.9336 g cm^{-3})⁵¹ would inhibit the damage caused by energetic particles on the surface⁶⁰. Salt minerals have lower vapor pressure than ice⁶¹, and therefore can be considered more structurally stable under vacuum at low temperatures. Bu et al.³⁷ have shown that at Ceres-relevant equatorial temperatures ($>200\text{ K}$) natron will dehydrate within 6 days, but under Ceres polar conditions ($<120\text{ K}$), it will be stable for ~ 300 years. Temperatures near to the plume vents are thought to be 140 K but this is highly dependent on assumed surface characteristics⁶², which will affect the stability of natron. However, if natron is identified near to the plume, it is likely recently deposited and therefore worthy of investigation.

Geochemical plausibility on Enceladus

Our observation of natron as the dominant carbonate phase in a Na-Cl-CO₃ ice is supported by the expected phase behaviour of the system at these temperatures⁶³. Na, Cl and CO₃ species have been measured in the plume⁸. There has been no detection of carbonate or chloride salts on the surface of Enceladus, however, Cassini VIMS (Visible and Infrared Mapping Spectrometer) did not have sufficient signal-to-noise to constrain salt abundance on the surface⁴⁵. The Cl:CO₃ ratio of our sample is comparable to plume measurements⁸ and our concentration is approximately 5 times higher to increase our ability to detect the crystallisation behaviour of natron. We expect concentration to impact ice microstructure and expect that inclusions would still be possible in lower concentrations, but that there would be fewer due to the lower total volume of salt that would precipitate. Large salt

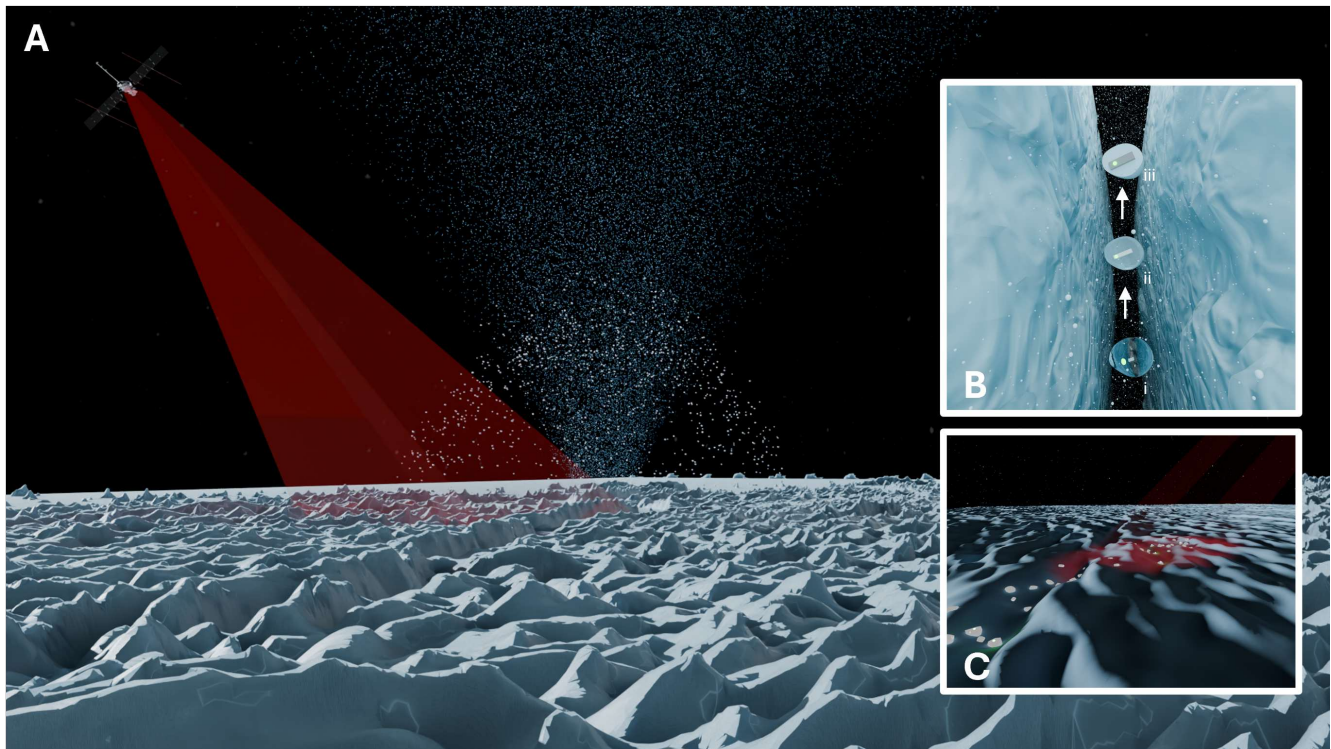


Figure 4. The vents of Enceladus could bring larger, natron-rich particles to the surface and deposit them in the areas surrounding the base of the plume. IR signatures of natron could be detected by remote observation (A). Entrapment of a biosignature in natron could potentially occur during freezing of a dispersed droplet (B). Signatures of natron should be identified via remote observation to identify sites of astrobiological interest (C)

173 crystals (up to 700 μm) of ikaite ($\text{CaCO}_3 \cdot 6\text{H}_2\text{O}$) have been found in sea ice with milimolar ocean salinity⁶⁴ and hydrohalite
 174 crystals of up to 100 μm have been found in 35 ppt NaCl ice⁶⁵. We therefore expect that the size of crystals we observe are not
 175 unique to high salinity solutions but their abundance would be reduced if the Enceladus ocean salinity is in a milimolar range²⁴.
 176 Higher concentration solutions may be generated where brine drainage is inhibited and cryo-concentration is effective. This
 177 could occur close to the surface during diapirism^{66,67}, intrusive events⁴³ or perhaps cryovolcanism⁶⁸. Due to natron's relatively
 178 low solubility, it precipitates early in the cryogenic sequence giving it a high potential to become trapped within ice compared
 179 to chloride salts that would remain soluble until the eutectic and could therefore drain with the brine phase under gravity. In
 180 these systems, larger natron crystals could potentially form and tectonic activity could lead to their exposure^{69,70}. This provides
 181 an alternative mechanism for bringing natron to the surface that is also applicable to ocean worlds where plumes have not been
 182 identified.

183 Conclusion

184 We have identified natron as an important solid component of the $\text{Na}-\text{Cl}-\text{CO}_3-\text{H}_2\text{O}$ system at low temperatures. The freezing
 185 of an Enceladus-type $\text{Na}-\text{Cl}-\text{CO}_3$ solution generates natron crystals that contain primary fluid inclusions. As inclusions have
 186 the potential to trap biological signatures present in subsurface fluids, we suggest that natron is a mineral of astrobiological
 187 importance in the solar system. Future missions to Enceladus and other carbonate bearing icy bodies should have the capability
 188 to characterise surface mineralogy. This capability should then be used to identify sites that contain natron as a priority due to
 189 its potential to trap liquid and potentially signatures of life if they are present. Future work should explore the potential for
 190 other low-solubility cryogenic salts to form inclusions; the impact of deformation as would happen during subsurface transport;
 191 and the impact of exposure to vacuum at the surface.

192 **Methods**

193 **Dual Imaging and Diffraction**

194 Dual imaging (μ CT) and diffraction (XRD) measurements were collected on the K11-DIAD beamline at Diamond Light
195 Source, UK. DIAD's unique capabilities come from its two independently configurable X-ray beams allowing for image-guided,
196 spatially-registered diffraction and imaging measurements.

197 An Na-Cl-H₂O solution was synthesised gravimetrically using 1.0 M/kg NaCl and 0.5 M/kg Na₂CO₃ in 40 g of deionised
198 (18 M Ω) water. The solution was then loaded into a 1 mm Kapton capillary. The temperature, controlled with a cryostream
199 (Oxford Cryosystems 800 series), was first set to 200 K and then warmed to 270 K to allow for partial melting of the ice in the
200 field of view; this annealing method allowed us to avoid issues with kinetics from nucleation inhibition. The solution was then
201 step-cooled to 200 K at 6 K/minute with tomography and diffraction measurements taken every 0.5 K up to 250 K and then
202 every 5 K down to 200 K.

203 Full tomographs containing 1005 projections were collected across 180° with a monochromatic (20 keV) X-ray beam, and a
204 0.1 s exposure using a PCO-Edge 5.5 detector. The imaged field of view was 1.2 x 1.4 mm with the total reconstructed sample
205 volume being 1.65 mm³. The detector was binned twice to increase collection speed (102 s per scan), giving a pixel resolution
206 of 2.16 μ m per voxel. Ten dark and flat-field projections were collected at the start and end to normalize the images before
207 reconstruction. Imaging datasets were reconstructed using Filtered Back Projection (ASTRA-Toolbox) through SAVU⁷¹.

208 Diffraction measurements were taken using a beam energy of 20 keV and a micro-focused spot size of 25x25 μ m. 2D
209 diffraction patterns were collected for 15 seconds using a Pilatus 2M area detector. DIAD's diffraction beam is collimated
210 using a flat and bending mirror pair and the wavelength is selected using a double crystal monochromator. The beam is then
211 directed and focused onto the sample position using a Kirkpatrick-Baez mirror system. This moving beam set up allows
212 the diffraction measurements to be spatially registered with the imaging field of view and uniquely allows for image-guided
213 diffraction. DIAD's geometry requires that only an arc of the Debye-Scherrer rings can be collected (Figure 1D).

214 **Data Processing**

215 Diffraction data were automatically azimuthally integrated and corrected for DIAD's moving beam geometry⁷². Pawley
216 refinements for phase identification were carried out in TOPAS 7 Academic. Patterns were refined using parameters from
217 published patterns⁷³⁻⁷⁵.

218 Imaging datasets were pre-processed to improve the results of segmentation. Datasets were binned 2 times and both a
219 bilateral filter and non-local means denoising filter were applied. Datasets were then segmented using a combination of a
220 U-Net_plus_plus with pre-trained resnet50 encoders, using Volume Segmantics⁷⁶, and manual segmentation in Avizo. A single
221 model was trained on 5 labelled volumes of 256 px³ across the series of tomographies taken. BCEDiceLoss criteria were used
222 with a DiceCoefficient as the metric. Size, shape, orientation and volume fractions were calculated using Avizo morphometric
223 implementations. Surfaces were generated and simplified in Avizo and then rendered in Blender 3.0.

224 **Data availability**

225 A full reconstructed tomography and processed diffraction 10x10 grid scan, used in this study, can be found in the Zenodo
226 repository: 10.5281/zenodo.17944439. All other data is available from the corresponding author on request.

227 **Acknowledgements**

228 JLH was partially funded by the Rutherford Appleton Laboratory and Faraday Institution through his emerging leader fellowship,
229 FIELF001, and by Research England's 'Expanding Excellence in England' grant through the "Multi-scale Multi-disciplinary
230 Modelling for Impact" program (M³4Impact).

231 The authors would like to acknowledge Diamond Light Source for access to the DIAD beamline under proposal MG31838
232 and MG38841.

233 **Author contributions statement**

234 Conceptualization: LP

235 Methodology: LP, JLH, SD, ST

236 Investigation: LP, JLH, AL, SD, ST

237 Visualization: LP

238 Writing: LP, JLH, AL, SD, ST

239 Competing interests

240 The authors declare no competing interests.

241 References

- 242 1. Porco, C. C. *et al.* Cassini observes the active south pole of Enceladus. *Science* **311**, 1393–1401 (2006).
- 243 2. Crow-Willard, E. N. & Pappalardo, R. T. Structural mapping of Enceladus and implications for formation of tectonized
244 regions. *J. Geophys. Res. Planets* **120**, 928–950 (2015).
- 245 3. Hansen, C. J. *et al.* Enceladus’ water vapor plume. *Science* **311**, 1422–1425 (2006).
- 246 4. Dougherty, M. K. *et al.* Identification of a dynamic atmosphere at Enceladus with the Cassini magnetometer. *Science* **311**,
247 1406–1409 (2006).
- 248 5. Nimmo, F., Porco, C. & Mitchell, C. Tidally modulated eruptions on Enceladus: Cassini ISS observations and models. *The*
249 *Astron. J.* **148**, 46 (2014).
- 250 6. Waite, J. H., Jr *et al.* Cassini ion and neutral mass spectrometer: Enceladus plume composition and structure. *Science* **311**,
251 1419–1422 (2006).
- 252 7. Waite, J. H. *et al.* Cassini finds molecular hydrogen in the Enceladus plume: Evidence for hydrothermal processes. *Science*
253 **356**, 155–159 (2017).
- 254 8. Postberg, F., Schmidt, J., Hillier, J., Kempf, S. & Srama, R. A salt-water reservoir as the source of a compositionally
255 stratified plume on Enceladus. *Nature* **474**, 620–622 (2011).
- 256 9. Khawaja, N. *et al.* Low-mass nitrogen-, oxygen-bearing, and aromatic compounds in Enceladean ice grains. *Mon. Notices*
257 *Royal Astron. Soc.* **489**, 5231–5243 (2019).
- 258 10. Postberg, F. *et al.* Detection of phosphates originating from Enceladus’s ocean. *Nature* **618**, 489–493 (2023).
- 259 11. Thomas, P. C. *et al.* Enceladus’s measured physical libration requires a global subsurface ocean. *Icarus* **264**, 37–47 (2016).
- 260 12. Nimmo, F., Spencer, J. R., Pappalardo, R. T. & Mullen, M. E. Shear heating as the origin of the plumes and heat flux on
261 Enceladus. *Nature* **447**, 289–291 (2007).
- 262 13. Le Gall, A. *et al.* Thermally anomalous features in the subsurface of Enceladus’s south polar terrain. *Nat. Astron.* **1**,
263 657–663 (2017).
- 264 14. O’Neill, C. & Nimmo, F. The role of episodic overturn in generating the surface geology and heat flow on Enceladus. *Nat.*
265 *Geosci.* **3**, 88–91 (2010).
- 266 15. Abramov, O. & Spencer, J. R. Endogenic heat from Enceladus’ south polar fractures: New observations, and models of
267 conductive surface heating. *Icarus* **199**, 189–196 (2009).
- 268 16. Neveu, M. *et al.* Returning samples from enceladus for life detection (2020).
- 269 17. Vincent, L. N., Fayolle, E. C., Hodyss, R., Johnson, P. V. & Noell, A. C. Bacterial spore morphology remains highly
270 recognizable after exposure to simulated enceladus and europa surface conditions. *Commun. Earth Environ.* **5** (2024).
- 271 18. Choukroun, M. *et al.* Sampling plume deposits on enceladus’ surface to explore ocean materials and search for traces of
272 life or biosignatures. *Planet. Sci. J.* **2** (2021).
- 273 19. Roedder, E. *Fluid Inclusions*, vol. 12 (De Gruyter, Berlin, 1984).
- 274 20. Goldstein, R. H. Fluid inclusions in sedimentary and diagenetic systems. *Lithos* **55**, 159–193 (2001).
- 275 21. McGenity, T. J., Gemmell, R. T., Grant, W. D. & Stan-Lotter, H. Origins of halophilic microorganisms in ancient salt
276 deposits. *Environ. Microbiol.* **2**, 243–250 (2000).
- 277 22. Schreder-Gomes, S. I., Benison, K. C. & Bernau, J. A. 830-million-year-old microorganisms in primary fluid inclusions in
278 halite. *Geology* **50**, 918–922 (2022).
- 279 23. Fang, Z., Knoll, P., McMahan, S., Qin, L. & Cockell, C. S. Preservation of microorganisms (*Chroococciopsis* sp. 029) in
280 salt minerals under low atmospheric pressure: Application to life detection on Mars. *The Planet. Sci. J.* **5**, 133 (2024).
- 281 24. Postberg, F. *et al.* Sodium salts in E-ring ice grains from an ocean below the surface of Enceladus. *Nature* **459**, 1098–1101
282 (2009).
- 283 25. McCoy, T. J. *et al.* An evaporite sequence from ancient brine recorded in Bennu samples. *Nature* **637**, 1072–1077 (2025).

- 284 **26.** Matsumoto, T. *et al.* Sodium carbonates on Ryugu as evidence of highly saline water in the outer Solar System. *Nat.*
285 *Astron.* 1–8 (2024).
- 286 **27.** Carrozzo, F. G. *et al.* Nature, formation, and distribution of carbonates on Ceres. *Sci. Adv.* **4**, e1701645 (2018).
- 287 **28.** Cartwright, R. J. *et al.* JWST reveals CO ice, concentrated CO₂ deposits, and evidence for carbonates potentially sourced
288 from Ariel’s interior. *The Astrophys. J. Lett.* **970**, L29 (2024).
- 289 **29.** Marion, G. M. Carbonate mineral solubility at low temperatures in the Na-K-Mg-Ca-H-Cl-SO₄-OH-HCO₃-CO₃-CO₂-H₂O
290 system. *Geochimica et Cosmochimica Acta* **65**, 1883–1896 (2001).
- 291 **30.** Glen, J. W. & Perutz, M. F. The growth and deformation of ice crystals. *J. Glaciol.* **2**, 397–403 (1954).
- 292 **31.** Cole, D. M. The microstructure of ice and its influence on mechanical properties. *Eng. Fract. Mech.* **68**, 1797–1822 (2001).
- 293 **32.** Pawley, G. S. Unit-cell refinement from powder diffraction scans. Tech. Rep. (1981).
- 294 **33.** Qi, C., Stern, L. A., Pathare, A., Durham, W. B. & Goldsby, D. L. Inhibition of grain boundary sliding in fine-grained ice
295 by intergranular particles: Implications for planetary ice masses. *Geophys. Res. Lett.* **45**, 12–757 (2018).
- 296 **34.** Hooke, R. L., Dahlin, B. B. & Kauper, M. T. Creep of ice containing dispersed fine sand. *J. Glaciol.* **11**, 327–336 (1972).
- 297 **35.** Wilson, C. J. L., Hunter, N. J. R., Luzin, V., Peternell, M. & Piazzolo, S. The influence of strain rate and presence of
298 dispersed second phases on the deformation behaviour of polycrystalline D₂O ice. *J. Glaciol.* **65**, 101–122 (2019).
- 299 **36.** Timco, G. W. & Weeks, W. F. A review of the engineering properties of sea ice. *Cold Reg. Sci. Technol.* **60**, 107–129
300 (2010).
- 301 **37.** Bu, C. *et al.* Stability of hydrated carbonates on Ceres. *Icarus* **320**, 136–149 (2019).
- 302 **38.** Bland, M. T. *et al.* Composition and structure of the shallow subsurface of Ceres revealed by crater morphology. *Nat.*
303 *Geosci.* **9**, 538–542 (2016).
- 304 **39.** Pamerleau, I. F., Sori, M. M. & Scully, J. E. C. An ancient and impure frozen ocean on Ceres implied by its ice-rich crust.
305 *Nat. Astron.* **8**, 1373–1379 (2024).
- 306 **40.** Schurmeier, L. & Dombard, A. J. Unrelaxed craters muddy the waters of the dwarf planet Ceres (2024).
- 307 **41.** Sekine, Y. *et al.* High-temperature water-rock interactions and hydrothermal environments in the chondrite-like core of
308 Enceladus. *Nat. Commun.* **6** (2015).
- 309 **42.** Hsu, H. W. *et al.* Ongoing hydrothermal activities within Enceladus. *Nature* **519**, 207–210 (2015).
- 310 **43.** Souček, O., Běhouňková, M., Lanzendörfer, M., Tobie, G. & Choblet, G. Variations in plume activity reveal the dynamics
311 of water-filled faults on Enceladus. *Nat. Commun.* **15**, 2029 (2024).
- 312 **44.** Hedman, M. M. *et al.* An observed correlation between plume activity and tidal stresses on Enceladus. *Nature* **500**,
313 182–184 (2013).
- 314 **45.** Postberg, F. *et al.* Plume and surface composition of Enceladus. In *Enceladus and the Icy Moons of Saturn*, 141–174 (The
315 University of Arizona Press, 2018).
- 316 **46.** Porco, C. C., Dones, L. & Mitchell, C. Could it be snowing microbes on Enceladus? assessing conditions in its plume and
317 implications for future missions. *Astrobiology* **17**, 876–901 (2017).
- 318 **47.** Perera, L. J. & Cockell, C. S. Dispersion of bacteria by low-pressure boiling: Life detection in Enceladus’ plume material.
319 *Astrobiology* **23**, 269–279 (2023).
- 320 **48.** Klenner, F. *et al.* How to identify cell material in a single ice grain emitted from Enceladus or Europa. *Sci. Adv.* **10**,
321 ead10849 (2024).
- 322 **49.** Goldstein, D. B. *et al.* Enceladus plume dynamics: from surface to space. *Enceladus Icy Moons Saturn* 175–185 (2018).
- 323 **50.** Dong, Y., Hill, T. W. & Ye, S. Y. Characteristics of ice grains in the Enceladus plume from Cassini observations. *J.*
324 *Geophys. Res. Space Phys.* **120**, 915–937 (2015).
- 325 **51.** Jaumann, R. *et al.* Distribution of icy particles across Enceladus’ surface as derived from Cassini-VIMS measurements.
326 *Icarus* **193**, 407–419 (2008).
- 327 **52.** Degruyter, W. & Manga, M. Cryoclastic origin of particles on the surface of Enceladus. *Geophys. Res. Lett.* **38** (2011).
- 328 **53.** Blättler, C. L. Examining uncertainties in major-ion reconstructions of seawater from halite fluid inclusions. *Earth-Science*
329 *Rev.* **264**, 105142 (2025).

- 330 **54.** Chi, G., Diamond, L. W., Lu, H., Lai, J. & Chu, H. Common problems and pitfalls in fluid inclusion study: A review and
331 discussion. *Minerals* **11**, 7 (2021).
- 332 **55.** Shanina, S. N., Galamay, A. R., Ignatovich, O. O., Burdelnaya, N. S. & Valyaeva, O. V. Organic matter of the salt sequence
333 in the southern part of the Yakshinskoe potassium–Magnesium salt deposit. *Geochem. Int.* **56**, 719–734 (2018).
- 334 **56.** Pellegrino, L. *et al.* The impact of early diagenesis on biosignature preservation in sulfate evaporites: Insights from
335 Messinian (late Miocene) gypsum. *Geobiology* **22**, e12595 (2024).
- 336 **57.** Benison, K. C., Hallsworth, J. E., Zalar, P., Glavina, M. & Gunde-Cimerman, N. Extremophilic and common fungi in acid
337 brines and their halite. *Extremophiles* **29**, 15 (2025).
- 338 **58.** Stan-Lotter, H. *et al.* *Halococcus dombrowskii* sp. nov., an archaeal isolate from a Permian alpine salt deposit. *Int. J. Syst.*
339 *Evol. Microbiol.* **52**, 1807–1814 (2002).
- 340 **59.** Gill, K. K., Jagniecki, E. A., Benison, K. C. & Gibson, M. E. A Mars-analog sulfate mineral, mirabilite, preserves
341 biosignatures. *Geology* **51**, 818–822 (2023).
- 342 **60.** Kotova, A., Roussos, E., Kollmann, P., Krupp, N. & Dandouras, I. Galactic cosmic rays access to the magnetosphere of
343 Saturn. *J. Geophys. Res. Space Phys.* **124**, 166–177 (2019).
- 344 **61.** Chase, M. W. *et al.* JANAF thermochemical tables - 3rd edition .1. Al-Co. *J. Phys. Chem. Ref. Data* **14**, 1–926 (1985).
- 345 **62.** Spencer, J. R. *et al.* Cassini encounters Enceladus: Background and the discovery of a south polar hot spot. *Science* **311**,
346 1401–1405 (2006).
- 347 **63.** Linke, W. F. *Solubilities: Inorganic and Metal-Organic Compounds*, vol. II (American Chemical Society, Washington, DC,
348 1958), 4th edn.
- 349 **64.** Rysgaard, S. *et al.* Ikaite crystal distribution in winter sea ice and implications for CO₂ system dynamics. *The Cryosphere*
350 **7**, 707–718 (2013).
- 351 **65.** Light, B., Brandt, R. E. & Warren, S. G. Hydrohalite in cold sea ice: laboratory observations of single crystals, surface
352 accumulations, and migration rates under a temperature gradient, with application to “snowball earth”. *J. Geophys. Res.*
353 *Ocean.* **114** (2009).
- 354 **66.** Nimmo, F. & Pappalardo, R. T. Diapir-induced reorientation of Saturn’s moon Enceladus. *Nature* **441**, 614–616 (2006).
- 355 **67.** Schenk, P. M. & McKinnon, W. B. New global topography of Enceladus: Hypsometry, basins, spherical harmonics, shell
356 thickness, and true polar wander revisited. *Icarus* **408**, 115851 (2024).
- 357 **68.** Quick, L. C. *et al.* A possible brine reservoir beneath Occator crater: Thermal and compositional evolution and formation
358 of the Cerealia dome and Vinalia faculae. *Icarus* **320**, 119–135 (2019).
- 359 **69.** Rossi, C., Cianfarra, P., Salvini, F., Bourgeois, O. & Tobie, G. Tectonics of Enceladus’ south pole: Block rotation of the
360 tiger stripes. *J. Geophys. Res. Planets* **125**, e2019JE006242 (2020).
- 361 **70.** Kargel, J. S. & Pozio, S. The volcanic and tectonic history of Enceladus. In *Lunar and Planetary Science Conference*,
362 vol. 27, 645 (1996).
- 363 **71.** Wadeson, N. & Basham, M. Savu: A Python-based, MPI framework for simultaneous processing of multiple, N-
364 dimensional, large tomography datasets. In *2016 12th International Conference on eScience*, 281–290 (IEEE, 2016).
- 365 **72.** Leonardi, A. *et al.* The moving-beam diffraction geometry: the DIAD application of a diffraction scanning probe. *J. Appl.*
366 *Crystallogr.* **59** (2026).
- 367 **73.** Klewe, B. & Pedersen, B. The crystal structure of sodium chloride dihydrate. *Acta Crystallogr. Sect. B: Struct. Crystallogr.*
368 *Cryst. Chem.* **30**, 2363–2371 (1974).
- 369 **74.** Fortes, A. D. *et al.* No evidence for large-scale proton ordering in Antarctic ice from powder neutron diffraction. *The J.*
370 *Chem. Phys.* **120**, 11376–11379 (2004).
- 371 **75.** Taga, T. Crystal structure of Na₂CO₃·10H₂O. *Acta Crystallogr. Sect. B: Struct. Crystallogr. Cryst. Chem.* **25**, 2656–2657
372 (1969).
- 373 **76.** King, O. N. F., Bellos, D. & Basham, M. Volume segmantics: A Python package for semantic segmentation of volumetric
374 data using pre-trained PyTorch deep learning models. *J. Open Source Softw.* **7**, 4691 (2022).